International Journal of Applied Earth Observation and Geoinformation 59 (2017) 9–18

Contents lists available at ScienceDirect

International Journal of Applied Earth Observation and Geoinformation

journal homepage: www.elsevier.com/locate/jag

Polarimetric differential SAR interferometry in an arid natural environment

Adugna G. Mullissa[a,*], Valentyn Tolpekin[a], Alfred Stein[a], Daniele Perissin[b]

[a] Department of Earth Observation Science, Faculty of Geoinformation Science and Earth Observation, University of Twente, P.O. Box 217, 7500AE Enschede, The Netherlands
[b] Lyle School of Civil Engineering, Purdue University, 550 Stadium Mall Drive, West Lafayette, IN 47907, USA

ARTICLE INFO

Article history:
Received 14 July 2016
Received in revised form 11 February 2017
Accepted 21 February 2017
Available online 8 March 2017

Keywords:
Polarimetric optimization
Differential SAR interferometry (DInSAR)
Polarimetric SAR interferometry (PolInSAR)
GPS

ABSTRACT

Ground deformation measurements have contributed to a better understanding of the processes and mechanisms involved in natural hazards. Those include landslides, subsidence, earthquakes and volcanic eruptions. Spaceborne Differential Interferometric Synthetic Aperture RADAR (DInSAR) is a well studied technique for measuring ground deformation. Quality of deformation measurements, however, is often degraded by decorrelation. With the advent of fully polarimetric SAR satellite sensors, polarimetric optimization techniques exploiting polarimetric diversity improve the phase quality of interferograms. In this paper, we analyzed three polarimetric optimization methods to determine the optimal one for application in an arid natural environment. We considered coherence decomposition in single and double phase center scenarios. Coherence estimation bias associated with each optimization method has been analyzed. We compared the derived displacement values with terrestrial GPS measurements. The study shows that polarimetric optimization increases the number of coherent pixels by upto 6.89% as compared with a single polarization channel. The study concludes that polarimetric optimization coupled with DInSAR analysis yields more reliable deformation results in a low coherence region.

1. Introduction

The advent of Interferometric Synthetic Aperture Radar (InSAR) has improved the accuracy and efficiency of surface deformation measurements. In turn, these measurements have contributed to a better understanding of the processes and mechanisms involved in natural disasters such as landslides, subsidence, earthquakes and volcanic eruptions (Massonnet et al., 1993; Amelung et al., 2000). As useful as SAR interferometry can be, it is affected by temporal decorrelation, geometric decorrelations and atmospheric effects that all degrade interferometric phase quality (Zebker et al., 1992; Hanssen, 2001). This in turn, governs the quality of deformation measurements in differential interferometry.

Traditionally, interferometric phase quality is assessed by means of the coherence stability (Mora et al., 2003) and the amplitude dispersion index (Ferretti et al., 2001). Recently, with the launch of fully polarimetric SAR sensors like ALOS PALSAR (Rosenqvist et al., 2007), RADARSAT-2 (Morena et al., 2004) and TERRASAR-X (Buckreuss et al., 2003), studies were undertaken that utilize the polarimetric information to find the polarization state that can provide the highest interferometric phase quality in an InSAR data stack. Polarimetric interferometric coherence optimization (Cloude and Papathanassiou, 1998) assumes either a changing dominant scattering mechanism at each end of the baseline in an interferogram or a similar scattering mechanism. Examples are the MSM (Multiple scattering mechanism) and the ESM (Equal scattering mechanism) (Colin et al., 2006). Both MSM and ESM algorithms were extended from a single baseline to include multi-baselines (Neumann et al., 2008).

Multi-baseline coherence optimization in the context of differential interferometry was introduced in Pipia et al. (2009). Navarro-Sanchez et al. (2010) and Navarro-Sanchez and Lopez-Sanchez (2012) applied polarimetric optimizations on dual polarized TERRASAR-X data to increase the number of persistent scatterer candidate points in both the amplitude stability index and the average coherence. Navarro-Sanchez et al. (2014) and Iglesias et al. (2014) compared polarimetric optimization methods to both the amplitude dispersion index and the coherence stability index in the context of permanent scatterer interferometry (PSI) using fully polarized RADARSAT-2 data. Recently, Wu et al. (2015) improved the computational efficiency of polarimetric coherence optimization by changing the four parameter optimization problem into two

* Corresponding author.
E-mail addresses: a.mullissa@utwente.nl (A.G. Mullissa), v.a.tolpekin@utwente.nl (V. Tolpekin), a.stein@utwente.nl (A. Stein), perissin@purdue.edu (D. Perissin).

http://dx.doi.org/10.1016/j.jag.2017.02.019
0303-2434/

independent optimization problems with two parameters each. Most literature on polarimetric optimization from space-borne repeat pass configuration have applied differential interferometry to urban areas (Pipia et al., 2009; Navarro-Sanchez et al., 2014; Iglesias et al., 2014). Validation was done qualitatively by comparing coherence improvements with different optimization methods. As an exception Navarro-Sanchez et al. (2010) and Alipour et al. (2015) applied polarimetric optimization in a rural setting.

The novelty of the current work is threefold. First, we apply coherence decomposition analysis of optimized coherences in single and double phase center scenarios for potential estimation of deformation under a vegetation canopy. Second, we combine coherence and phase bias associated with three coherence optimization methods. Third we compare the deformation as estimated from coherence optimization with terrestrial GPS measurements.

The objective of this paper was to assess, evaluate and validate polarimetric optimization for DInSAR application in an arid natural environment. The study area was located in the Ethiopian rift valley and both quad polarized and dual polarized images were applied.

2. Test area and datasets

This study focuses on the Ethiopian section of the East African rift valley. The study area has received scientific attention in the past because of its suitability for studying the role of crustal extensions and magmatism when rifting progresses to sea-floor spreading (Hammond et al., 2011). Hence, it was selected to evaluate polarimetric optimization for DInSAR applications in a natural environment. Within the study period the area has experienced dike intrusions followed by a medium level earthquake (Keir et al., 2011).

Three quad polarized ALOS PALSAR images and seven dual polarized images were used (Table 1). To avoid phase aliasing, the data were oversampled twice in range. The ALOS PALSAR sensor acquires data in L band for both quad and dual polarimetric data. It comprises 2400 × 13000 pixels and covers 24.3 km × 45.5 km in range and azimuth directions, respectively. It is a natural environment that consists of bare surface, sparsely vegetated area, densely vegetated area and smooth sandy surface. There are several GPS sites within the vicinity of the study area (Fig. 1), but most of the GPS points lack the temporal overlap between the image acquisition dates. The GPS stations with designation names Dabt, Datr, Da25 and 'Dayr' were used in this study.

Table 1
Acquisition parameters for the ALOS PALSAR quad and dual polarized data.

	Quad polarized data	Dual polarized data.
Satellite	ALOS-PALSAR (PLY)	ALOS-PALSAR (FBD)
Resolution	3.54 m × 11.55 m	3.2 m × 9 m
Incidence angle	23.92°	38.7°
Orbit	Ascending	Ascending
Temporal baseline	46 days	46 days
Dates	July 25, 2008–March 12, 2009	June 29, 2007–November 22, 2010
Number of images	3	7

3. Methodology

3.1. Polarimetric SAR interferometry

Fully polarimetric SAR data can be represented with the target scattering vector k using the Pauli basis, by assuming reciprocity.

$$k_i = \frac{1}{\sqrt{2}}\begin{bmatrix} S_{HH_i} + S_{VV_i} & S_{HH_i} - S_{VV_i} & 2S_{HV_i} \end{bmatrix}^T \quad (1)$$

In dual polarized SAR data, the target scattering vector k_i reduces to: $k_i = \frac{1}{\sqrt{2}}\begin{bmatrix} S_{HH_i} + S_{VV_i} & S_{HH_i} - S_{VV_i} \end{bmatrix}^T$ in TerraSAR-X configuration (HH VV) or $k_i = \begin{bmatrix} S_{HH_i} & 2S_{HV_i} \end{bmatrix}^T$ in ALOS PALSAR configuration (HH HV), where $i \in [1, 2, \ldots, n]$ is the image number for a multi-image acquisition. The polarization channels S_{XY} represent the horizontal (H) and vertical (V) polarization states which are indexed as X, $Y = (H, V)$ and ^{T} is the matrix transpose. The 6×6 Hermitian matrix T contains both the polarimetric information contained in each image and the interferometric information of each pair.

$$T = \langle kk^\dagger \rangle = \begin{bmatrix} T_{ii} & \Omega_{ij} \\ \Omega_{ij}^\dagger & T_{jj} \end{bmatrix}, \quad \text{with} \quad k = \begin{bmatrix} k_i^T & k_j^T \end{bmatrix}^T. \quad (2)$$

where † denotes a matrix conjugate transpose and $\langle\rangle$ represents the temporal or spatial averaging. T_{ii} and T_{jj} are the coherency matrices related to images i and j, $\Omega_{ij} (i \neq j)$ is the polarimetric

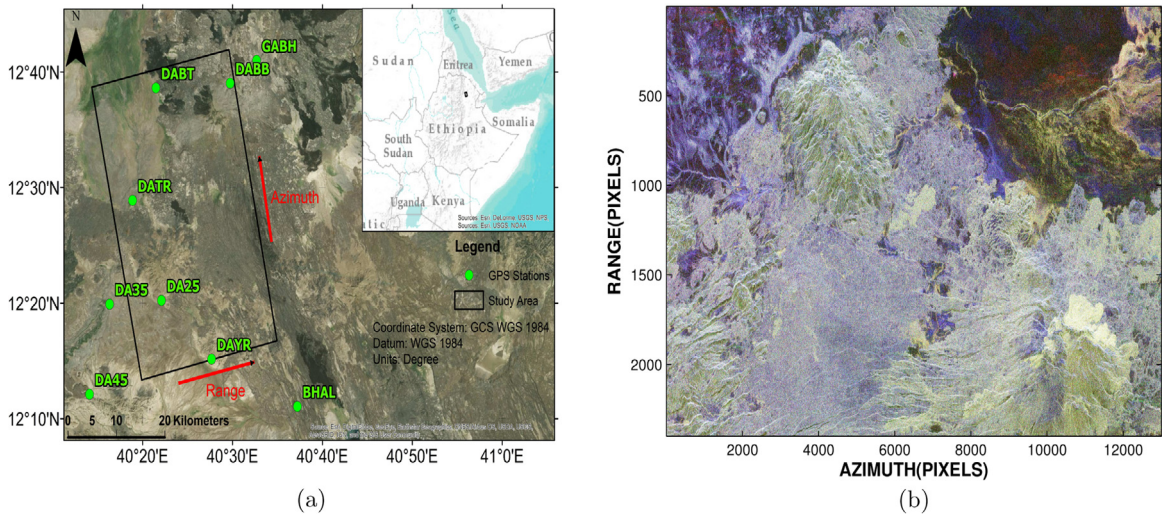

Fig. 1. (a) Location map of the study area obtained from Google Earth. The study area, covering an area of 138.24 km^2, was located in the Ethiopian section of the East African rift valley. (b) False color composite image for the study area (Blue stands for $|S_{HH} + S_{VV}|$, green stands for $|2S_{HV}|$ and red stands for $|S_{HH} - S_{VV}|$. (For interpretation of the references to colour in this figure legend, the reader is referred to the web version of this article.)

interferometric correlation matrix. The polarization dependent interferometric coherence is given as:

$$\gamma(\omega_i, \omega_j) = \mid \gamma \mid e^{i\phi} = \frac{\omega_i^{\dagger} \Omega_{ij} \omega_j}{\sqrt{(\omega_i^{\dagger} T_{ii} \omega_i)(\omega_j^{\dagger} T_{jj} \omega_j)}}. \quad (3)$$

In DInSAR applications the assumption $\omega_i = \omega_j = \omega$ is made to avoid arbitrary phase components that emerge from using two different scattering phase centres for each pair of images. Based on (3), coherence optimization aims to find a unitary projection vector ω that gives the highest interferometric coherence, i.e the polarization state that is least affected by decorrelation. In this study three coherence optimization methods, BEST (Iglesias et al., 2014), Joint diagonalization based optimization (JD) (Ferro-Famil et al., 2009; Navarro-Sanchez et al., 2014) and ESM (Colin et al., 2006; Neumann et al., 2008) are evaluated and compared with the HH channel.

3.2. Coherence decomposition

The interferometric coherence function can be decomposed into different decorrelation sources as:

$$\gamma = e^{i\phi} \gamma_{snr} \cdot \gamma_{temp} \cdot \gamma_{geo} \cdot \gamma_{vol}, \quad (4)$$

where γ_{snr} is decorrelation due to additive noise, γ_{temp} is temporal decorrelation relating to change in the scattering property of the scene, $\gamma_{geometric}$ is baseline decorrelation resulting from wave number shift due to different look angles. Note that $\gamma_{geometric}$ can be completely removed by range spectral filtering. Hence, the coherence function in a simplified form equals:

$$\gamma = e^{i\phi} \gamma_{snr} \cdot \gamma_{temp} \cdot \gamma_{vol}. \quad (5)$$

To evaluate the performance of coherence optimization in a natural environment we consider two scenarios: a resolution cell with a single phase center (surface scattering) and one with a double phase center (vegetation over ground).

3.2.1. Single phase center

In pure surface scattering, we assume little or no depolarization so we set $\gamma_{vol} = 1$. Hence, the polarization dependent coherence further simplifies to:

$$\gamma(\omega) = e^{i\phi} \gamma_{snr} \cdot \gamma_{temp}. \quad (6)$$

Moreover, temporal decorrelation does not affect the coherence in a polarization sensitive way. Hence, it is modelled as a scalar multiplier applied to all optimization results indicating that polarization plays a direct role in minimizing the signal to noise decorrelation.

3.2.2. Double phase center

In a vegetated region, coherence can be modelled using a two layer scattering model like the random volume over ground (RVoG) model (Papathanassiou and Cloude, 2001). By disregarding temporal and signal to noise decorrelation the polarization dependent complex interferometric coherence is given in the RVoG model as (Cloude, 2009):

$$\gamma(\omega) = e^{i\phi(z_0)} \left(\gamma_{vol} + \left(\frac{\mu(\omega)}{1 + \mu(\omega)} (1 - \gamma_{vol})\right)\right). \quad (7)$$

Here the volume decorrelation, γ_{vol} is a fixed complex number independent of polarization, $\mu(\omega)$ is the polarization dependent fraction of effective surface scattering and z_0 is the ground surface. Since the volume component is complex, variation occurs in the average differential phase and coherence amplitude. Hence, as discussed in the previous section, higher coherence amplitude indicates a higher signal to noise ratio. In vegetated regions, however, it contains vegetation bias and is no longer associated with the highest phase accuracy. The coherence function is a straight line if plotted in the complex plane with one end going through γ_{vol} and the other through $e^{i\phi(z_0)}$. The optimization method that presents a phase center closest to the ground and the highest signal to noise ratio is the best optimization method in vegetated regions.

For potential estimation of displacements under a canopy we first estimate the ground phase that is corrected for vegetation bias. This is derived using the three stage RVoG inversion (Cloude and Papathanassiou, 2003). In this method, a line is fitted through the coherences in the complex plane using total least squares. The fitted line crosses the unit circle in the complex plane twice and the ground phase is located at the intersection point closest to the low phase center. By assuming absence of temporal decorrelation we can apply three-image differential interferometry on the ground phase estimated from two different pairs of images to estimate ground deformation under a vegetation canopy.

3.3. Coherence bias

The interferometric coherence estimator, however, is biased and the magnitude of the bias depends upon the number of samples and the stationarity assumption (Touzi et al., 1999). To investigate this bias, we simulate single baseline PolInSAR data (Cloude, 2009). It starts with a known reference interferometric coherency matrix $\tilde{T}$, which is expressed using eigen decomposition as $\tilde{T} = U\Sigma U^{-1}$. Here U is a matrix containing eigenvectors arranged in columns and Σ is a diagonal matrix containing the corresponding eigenvalues (λ).

$$e = \begin{bmatrix} e_1 \\ . \\ . \\ e_n \end{bmatrix}, \quad \text{with} \quad e_j = \sqrt{\lambda_j} \left\{ G_a(0, 0.5) + iG_b(0, 0.5) \right\},$$

$$j \in [1, 2, \ldots, n]. \quad (8)$$

For single baseline PolInSAR data $n = 6$. We simulate the polarimetric interferometric target vector by first generating two independent Gaussian random sequences, G_a and G_b, with mean = 0 and variance = 0.5. Those are combined into a complex series followed by scaling it by the square root of the appropriate eigenvalue (8). Next, we generate k (2) by collecting this series into a vector e and introducing a complex correlation by multiplying this vector with the matrix of eigenvectors, i.e. $k = U \cdot e$. k follows a zero mean complex multivariate Gaussian probability density function.

3.4. GPS data processing

The GPS station data used for validation were obtained from UNAVCO's data archive interface (UNAVCO, 2016). First, station coordinates, atmospheric delay and Earth orientation parameters were calculated using double difference phase observations. The station daily solutions were calculated by least square adjustment of double difference phase observable obtained from each station. Next, the daily solutions were combined to estimate positions and repeatabilities for each station in the ITRF 2008 reference frame (Altamimi et al., 2011). Seven international GNSS service (IGS) GPS stations designated, 'Adis', 'Mali', 'Mbar', 'Mas1', 'Mal2', 'Nurk' and 'Nklg', were utilized to tie the position calculations to the international terresterial reference frame (ITRF 2008). A maximum normalized root mean square error of 0.3 was used to ensure the quality of the observations in time. The GPS data were processed using the GAMIT/GLOBK software suite (King and Bock, 2002).

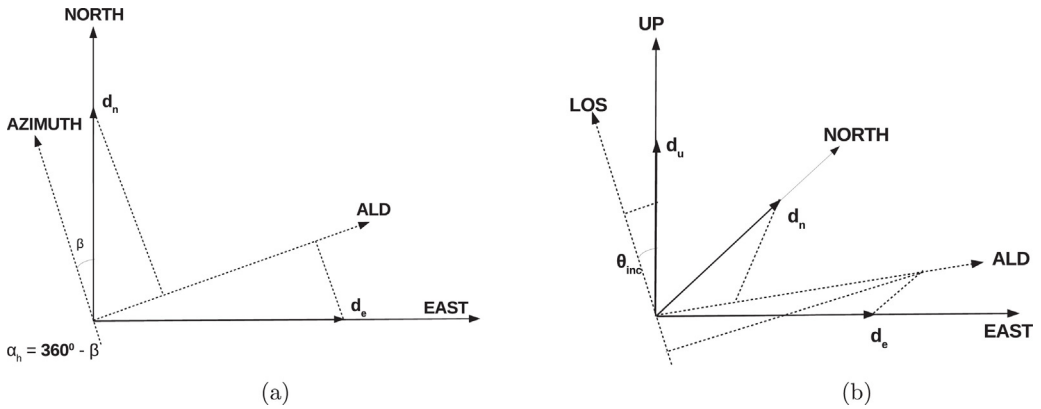

Fig. 2. Projection of LOS vector into its 3 dimensional components $[d_u d_e d_n]$. (a) Top view and (b) 3-D view. ALD refers to azimuth look direction (Hanssen, 2001).

The DInSAR line of sight (LOS) displacement vector for a right looking satellite is resolved to its displacement components (Fig. 2) (Hanssen, 2001) by

$$LOS = \left[\cos\theta_{inc}, \quad -\sin\theta_{inc}\cos(\alpha_h - \frac{3\pi}{2}), \quad \sin\theta_{inc}\sin(\alpha_h - \frac{3\pi}{2})\right] \times \left[d_u \quad d_e \quad d_n\right]^T. \tag{9}$$

where θ_{inc} is the incidence angle, α_h is the satellite azimuth vector and d_u, d_e and d_n are the LOS displacement components in the upward, eastern and northern directions, respectively. To compare the GPS measurements with LOS displacement the same equation was used to project the three dimensional GPS deformation measurements to the satellite LOS displacement vector using:

$$LOS_{gps} = \left[\cos\theta_{inc}, \ -\sin\theta_{inc}\cos(\alpha_h - \frac{3\pi}{2}), \ \sin\theta_{inc}\sin(\alpha_h - \frac{3\pi}{2})\right] \times \left[G_U \quad G_N \quad G_E\right]^T. \tag{10}$$

The LOS vector of $\left[0.914, \quad -0.08, \quad 0.3963\right]\left[G_U \quad G_N \quad G_E\right]^T$ is used to project the GPS data to in the LOS direction. Once the three dimensional GPS deformation was converted to the satellite LOS direction, it was compared with the LOS deformation derived from each of the three optimization methods.

4. Results

4.1. Coherence optimization

To assess the performance of coherence optimization we first compare the results of the coherence optimization for fully polarized data with coherence from the HH channel. To minimize bias when estimating the coherence, a 9×9 spatial averaging window was used to calculate the interferometric coherence values. A temporal average coherence was obtained by averaging the estimated coherence values along the time series of interferograms. To determine the pixel phase quality a threshold of 0.7 was used. Pixels with average coherence above the threshold present a phase standard deviation of less than 5° (Touzi et al., 1999).

The coherence amplitude histogram for different optimization methods is shown in Fig. 3. ESM selects the largest number of coherent pixels followed by JD and BEST (Table 2). Comparing the methods on their computational time, ESM requires 531% more time than HH, whereas JD requires 468% and BEST 232% more time than HH. Next, performance of coherence optimization methods is assessed for dual polarized data. To do so, dual polarization channels are synthesized from the quad polarized data. When using the TerraSAR-X channel configuration (HH VV), ESM provided the highest coherence followed by JD and BEST (Table 2). Clearly, the ALOS PALSAR configuration gives a slightly inferior result in coherence improvement as compared to the TERRASAR-X configuration. This is because in the presence of bare surface and sparse vegetation cover, the zero polarization phase difference in the HH + VV channel gives a higher signal to noise ratio than the HV channels. Overall, ESM achieves a higher coherence in both sparsely and densely vegetated surfaces but it achieves higher coherence improvements in bare and sparsely vegetated surfaces (Fig. 4). These results are consistent with other studies in rural settings (Navarro-Sanchez et al., 2010; Iglesias et al., 2015).

4.2. Coherence decomposition

The optimized complex coherences were plotted in the complex plane for bare surface and vegetated regions (Fig. 5). In bare and sparsely vegetated surfaces, the optimized coherences followed a radial pattern that is consistent with the single phase center scattering model. As a reference, we included the low and high phase centres following the phase diversity routine described in Tabb et al. (2002). ESM showed the highest coherence modulus followed by JD, BEST and HH while exhibiting similar differential phases that indicate higher signal to noise ratio. Hence, for bare and sparsely vegetated surfaces ESM is the best optimization method.

In vegetated areas, ESM again provided the highest coherence amplitude but its phase center showed a random pattern. In some areas it showed a phase center close to the ground whereas in other areas it showed the highest phase center when compared with the other techniques. This is because in the RVOG model the

Table 2
Number of coherent pixels selected using a coherence threshold $t = 0.7$ out of a total of 3.12×10^7 processed pixels for quad and dual polarized data in ALOS PALSAR configuration (HH and HV) and dual polarized data in TERRASAR-X configuration (HH and VV).

Method	QuadPol	DualPol (HH HV)	DualPol (HH VV)
$t = 0.7$			
HH	4.89%	4.89%	4.89%
BEST	7.32%	5.17%	7.10%
JD	8.70%	5.94%	8.33%
ESM	11.78%	6.77%	8.82%

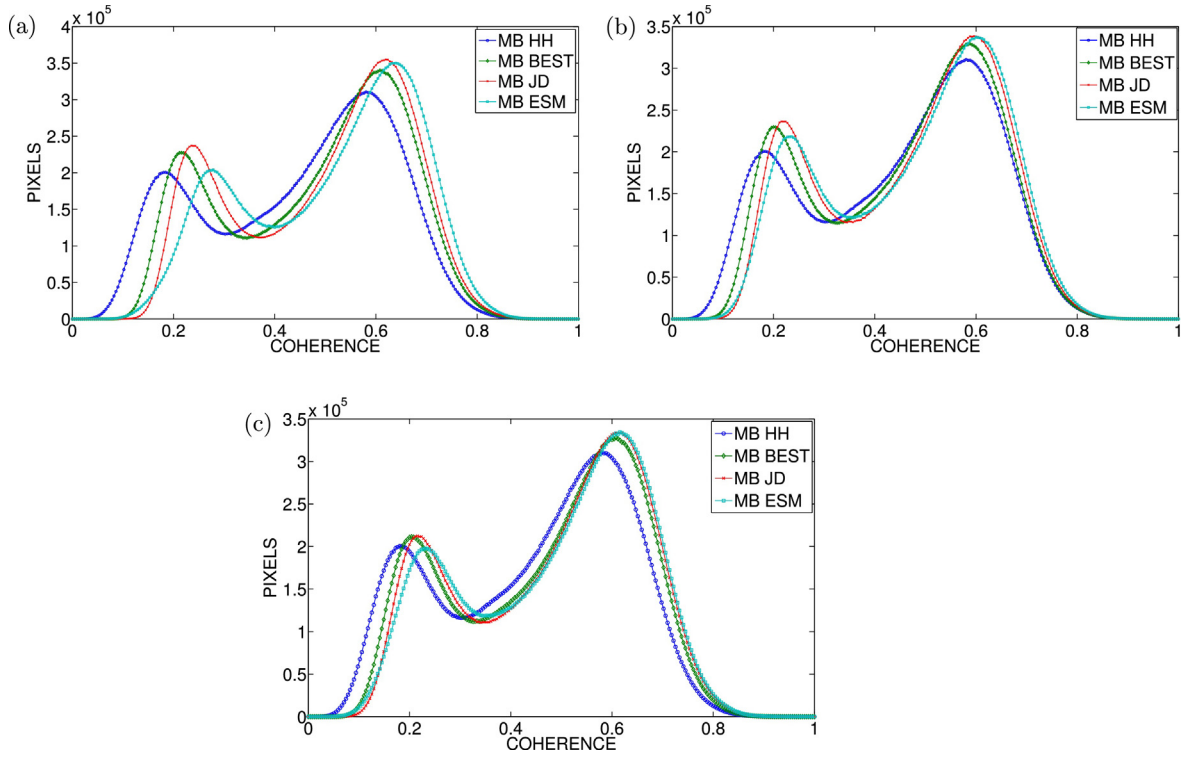

Fig. 3. Coherence histograms for different optimization methods (a) for quad polarized data, (b) for dual polarized data in ALOS configuration and (c) for dual polarized data in TERRASAR X configuration.

maximum coherence can be achieved in case of a minimum surface to volume scattering $\mu(\omega)$ or of a maximum surface to volume scattering $\mu(\omega)$. Hence, the optimization method that provides the highest coherence is not necessarily the one that is closest to the ground. The HH – VV channel commonly associated with double bounce scattering generally had a lower coherence amplitude than ESM optimized coherence but it consistently yielded a phase center closer to the ground than the other optimization techniques (Fig. 5b). In contrast, the HH + VV channel commonly associated with surface scattering had a higher phase center when compared with both HH – VV and HH channels. In vegetated areas with tree crown and trunks the HH – VV channel is dominant and achieves higher surface to volume scattering ratio with phase center very close to the ground. The HH + VV channel mostly scatters off the branches of a vegetation and does not achieve the highest surface to volume scattering ratio.

4.3. Coherence bias

To determine which optimization method is least affected by coherence estimation bias, we constructed a two reference polarimetric interferometric coherency matrices ($\tilde{T}$). The first ($\tilde{T}$) matrix has identity matrix for coherency matrix in images i and j, i.e. T_{ii} and $T_{jj} = I$, and Ω_{ij} is a diagonal matrix with $\Omega_{ij}(1,1) = 0.63 + 0.63i$, $\Omega_{ij}(2,2) = 0.49 + 0.49i$ and $\Omega_{ij}(3,3) = 0.35 + 0.35i$. The second ($\tilde{T}$) matrix has $T_{ii} = \begin{bmatrix} 9.4 & 0.4 - 0.6i & -0.7 - 0.3i \\ 0.4 + 0.6i & 2.4 & 0.2 - 0.02i \\ -0.7 + 0.3i & 0.2 + 0.02i & 0.8 \end{bmatrix}$,

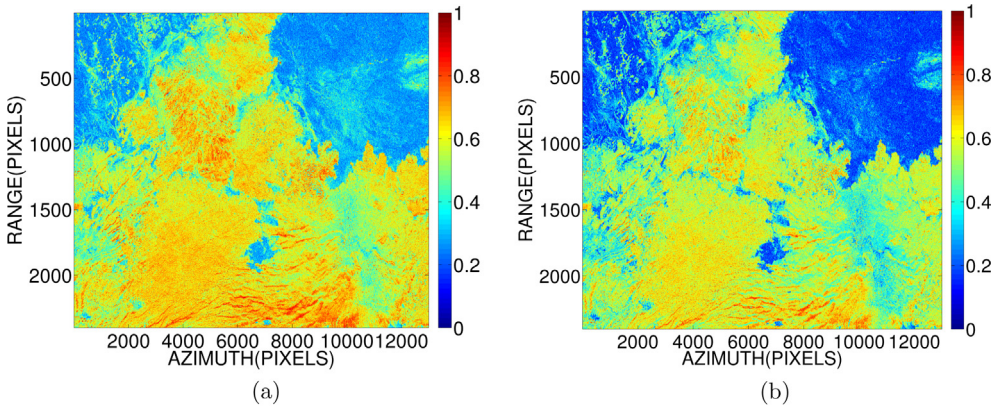

Fig. 4. The coherence amplitude for different cover types. ESM provided improvement in all cover types but its improvement is significant in sparsely vegetated areas. (a) ESM and (b) HH.

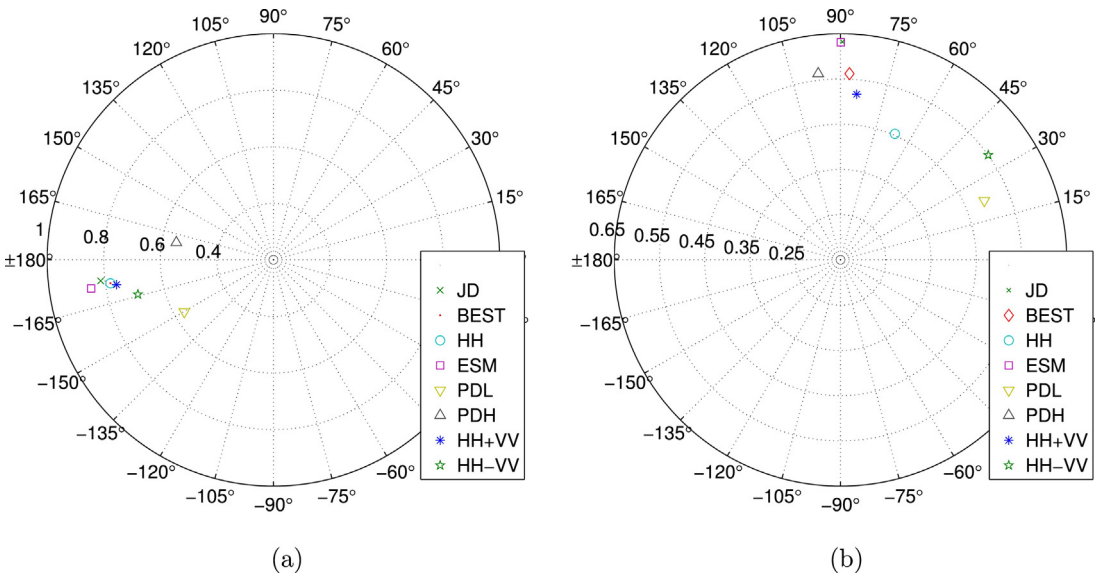

Fig. 5. Coherence loci for different optimization techniques for (a) bare and sparsely vegetated surfaces and (b) densely vegetated regions. PDL and PDH are the reference low phase center and high phase center, respectively.

$$T_{jj} = \begin{bmatrix} 9.0 & 1.1-0.6i & -0.4-0.3i \\ 1.1+0.6i & 2.05 & 0.06+0.06i \\ -0.4+0.3i & 0.06-0.06i & 0.7 \end{bmatrix} \quad \text{and} \quad \Omega_{ij} = \begin{bmatrix} 6.0-0.04i & 0.1-0.9i & -0.1-0.6i \\ 0.1+0.9i & 0.8+0.2i & 0.1+0.2i \\ -0.5+0.3i & 0.09+0.09i & 0.2+0.07i \end{bmatrix}.$$

Based on these matrices, two interferometric target scattering vectors k were simulated using the method discussed in Section 3.2 and the mean coherence for different number of looks was compared (Fig. 6). In both experiments ESM and BEST overestimated coherence whereas HH and JD underestimated coherence for small number of looks (less than 50 looks). For large number of looks (>70), ESM coherence converged to its true value. When using the same coherency matrices at each end of the baseline, coherence converged to its true value when using a large number of looks (typically >70). When the coherency matrices deviate slightly as depicted in the second experiment, ESM coherence converged to its true value for large number of looks, but JD failed to converge to its true value even for very large number of looks (>100). This indicates the sensitivity of JD to having similar coherency matrices at each end of the baseline. Moreover, if this condition is not fulfilled the coherence derived from it is always underestimated and biased. This effect is clearly shown by the differential phase error in Fig. 6d.

The coherence estimated for HH and BEST depends upon the polarization channel that provides the highest coherence. If the co-polar channels provide similar coherence values then both the HH and BEST converge to the true coherence value with a large number of looks. If the co-polar channels provide different coherency values the HH and BEST coherences show large differences. In Fig. 6c the VV channel provided significantly higher coherence than HH resulting in large differences between HH and BEST. Overall, the differential phase error is smallest for ESM followed by JD, BEST if the number of looks is large (>70) and if the coherency matrices are similar at each end of the baseline (Fig. 6b). If the coherency matrices are not similar at each end of the baseline, ESM still maintains the highest phase accuracy, whereas JD and BEST show phase errors in the estimated differential phases. With larger deviations between the coherency matrices, all optimization methods yield a low coherence and differential phases show large errors if compared to the true coherence. Hence, for the 81 looks utilized in this study and a coherence threshold of $t = 0.7$, ESM is the best polarimetric optimization method with the highest phase accuracy when using fully polarimetric SAR data.

4.4. Deformation measurement

Line of sight deformation maps were generated to obtain HH, BEST, JD and ESM interferograms. The optimized interferograms were unwrapped (Chen and Zebker, 2002) and converted to total displacement values following a standard DInSAR processing flow. Since the number of quad polarized data is low it was not possible to reliably correct for atmospheric, orbital and DEM errors. Pixels with temporally averaged coherence values <0.7 were masked (Fig. 7). Furthermore, the three dimensional GPS data were projected into the satellite LOS direction for comparison using (10). The LOS InSAR and GPS displacements were compared in terms of their deformation trend and correlation coefficient. For comparison it was not possible to find pixels that co-locate exactly with the GPS location. Hence, pixels with the nearest proximity to the GPS station and displacement standard deviation of <0.5 cm was used for the displacement comparison. The terresterial GPS measurement has an error of 0.14 cm, 0.12 cm, 0.27 cm and 0.12 cm at stations Dabt, Datr, Da25 and Dayr respectively. In the displacement data, a positive sign indicates LOS displacement towards the satellite and a negative sign indicates displacement away from the satellite.

The LOS displacement measured by the optimization methods followed a decreasing trend between July 25, 2008 and March 12, 2009 for station 'Dabt' and 'Datr' (Fig. 8). Whereas displacement at station 'Dayr' experienced an increasing trend in displacement values for all methods. This was due to two earthquake events occurring on October 17, 2008 and February 11, 2009 that was induced by dike injection (Keir et al., 2011). The displacement trend is consistent with the GPS data and available literature. Fig. 8 shows the displacement trend of ESM closely resembles the GPS data at nearly all stations. Furthermore, it showed the highest correlation coefficient (r) calculated by combining the different station measurements (Table 3). JD displacement correlation was lower than for BEST for quad and dual polarized data (HHHV) and for some stations displacement measurement least resembled the GPS data and other optimization methods (Fig. 8h and k). This is consistent with the phase bias analysis presented in Section 4.3. Atmospheric,

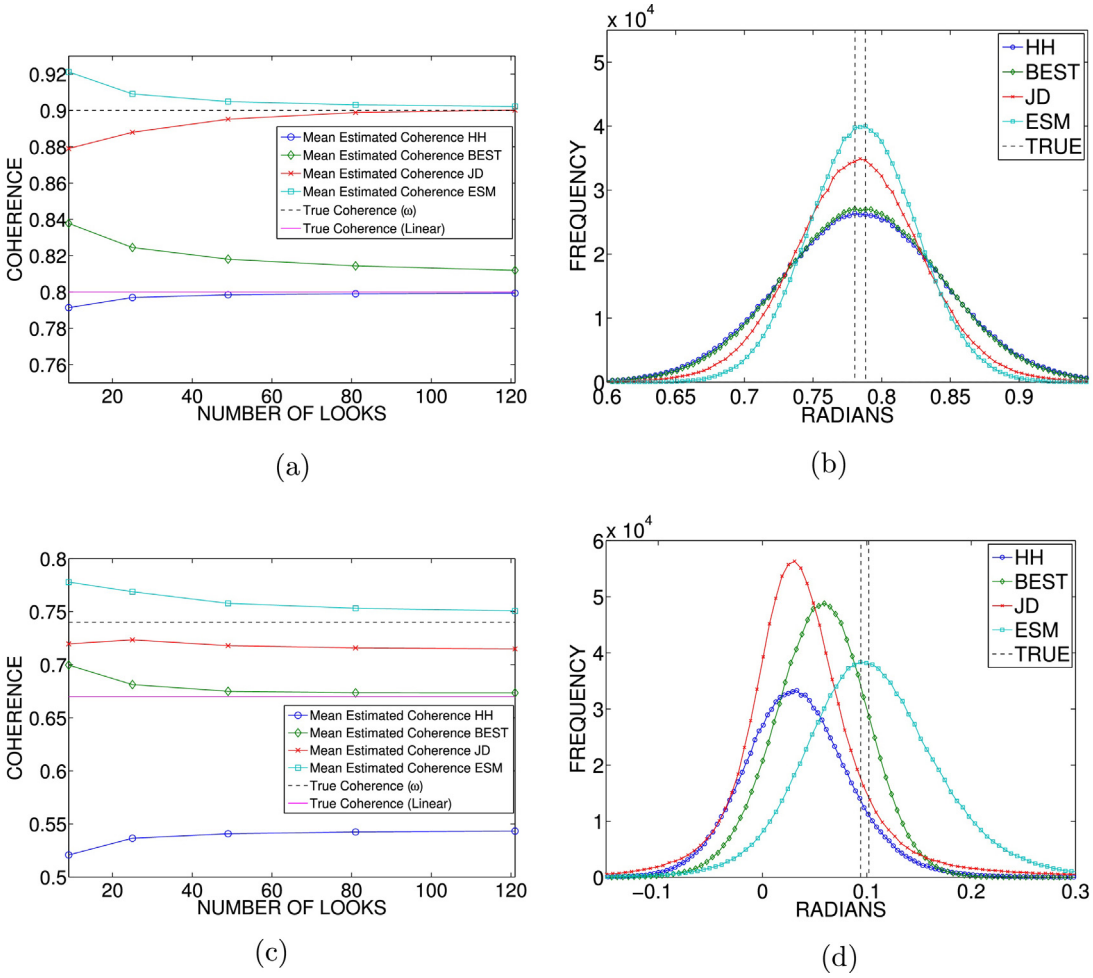

Fig. 6. (a) Coherence amplitude (mean of 10^6 realizations) of different optimization methods as a function of the number of looks, True coherence ω is the optimal coherence derived from the known coherency matrix with optimal projection vector and True coherence (Linear) is the optimal coherence calculated from the known coherency matrix using only HH, HV and VV channels. (b) Differential phases estimated from 81 looks for different optimization methods. (c) Coherence amplitude (mean of 10^6 realizations) of different optimization methods for second reference interferometric coherency matrix. (d) Differential phase estimated from 81 looks for different optimization methods.

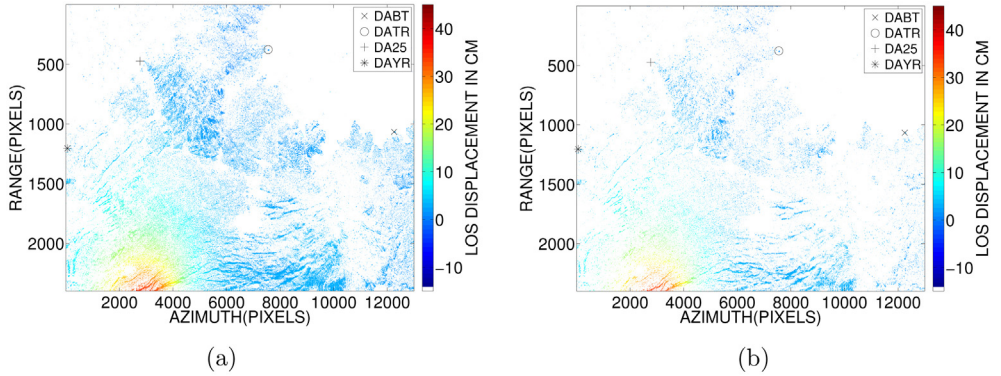

Fig. 7. Cumulative deformation maps derived from ESM (a) and the conventional HH channel (b) inbetween July 25, 2008 and March 12, 2009. Locations of the GPS stations are shown on the map.

orbital and DEM errors were not corrected and hence displacement estimates deviated from 0.25 cm to 1 cm from GPS measurements. Overall, ESM provided the highest accuracy in displacement estimation followed by JD, BEST and HH. In future work, the analysis should be extended to multi-temporal InSAR analysis (PS-InSAR) with more GPS stations, as this may improve the significance of the work.

5. Discussion

The study showed that ESM achieved the largest improvement in both bare and sparsely vegetated surfaces as compared to JD, BEST and conventional HH channel. ESM, however, is formulated based on the hypothesis of polarimetric stationarity. When this hypothesis is not fulfilled, ESM results in low temporal coherence

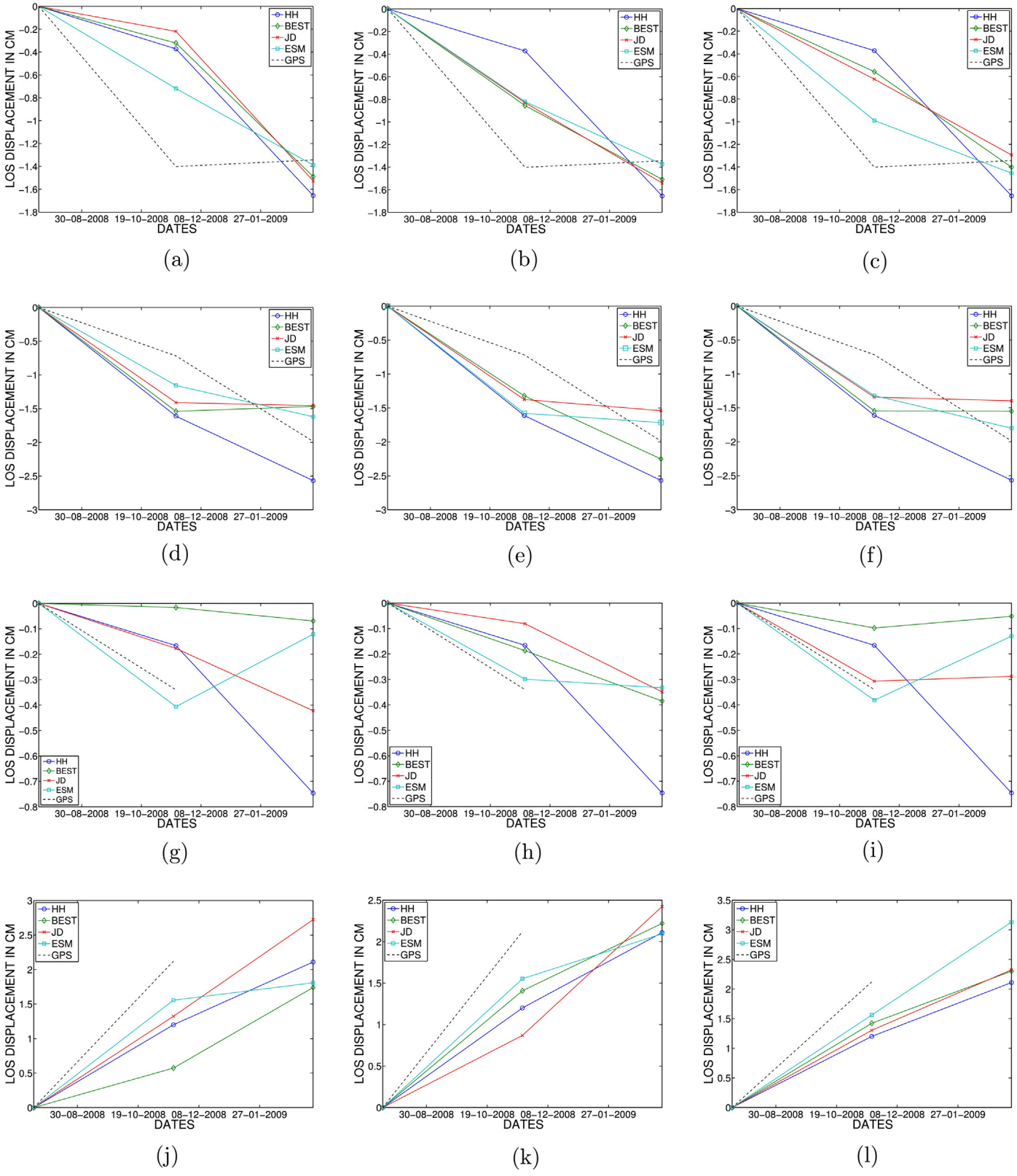

Fig. 8. Displacement time series derived from GPS and different optimization methods. Lines are included in the plot for illustration purposes. Rows display the stations Dabt, Datr, Da25 and Dayr, whereas the columns show Quad polarized, DualPol (HH HV) and DualPol (HH VV), respectively.

during optimization. It should be noted that even in this scenario it provides higher coherence than JD, BEST or HH (Fig. 3). However, it will most likely result in a low average coherence in the interferogram stack that is below the coherence threshold. Hence, coherence optimization has little additional value. In densely vegetated regions the coherency matrices at each end of the baseline differ significantly and therefore result in a relatively low differential phase accuracy and in a random phase center location. Hence,

Table 3
Pearson correlation coefficient (r) between different optimization methods and GPS data. Since a limited number of images are used to derive the displacement values, different stations are combined to derive the correlation coefficients. Displacement values corresponding with missing GPS data are not included in the calculation.

Method	QuadPol	DualPol (HH HV)	DualPol (HH VV)
HH	0.868	0.868	0.868
BEST	0.884	0.910	0.906
JD	0.871	0.898	0.927
ESM	0.961	0.937	0.967

in densely vegetation regions a polarization state that provides a phase center that is close to the ground surface should be used to derive displacement values. In this regard, HH-VV provides a phase center that is located closer to the ground surface as shown in Section 4.2 even-though it may select fewer coherent pixels than the optimization methods discussed in this paper. If trunk structure is absent within the vegetation canopy a coherence loci analysis should be performed to select the polarization state that selects a phase center that is closest to the ground surface. Moreover, to improve the optimization results, polarimetric stationarity can be mitigated by modelling the correlation between images based on their temporal and geometric baselines.

By using the RVoG model inversion it was possible to obtain the ground phase by removing the vegetation bias. The ground phase is useful to obtain geophysical parameters such as ground topography under vegetation canopy. In theory, the ground topography extracted from RVoG inversion also includes deformation signals. Therefore it is possible to estimate ground deformation under a forest canopy by removing the ground topography using repeat pass space-borne interferometry. In this study, due to the long temporal baseline, the signal was affected by temporal decorrelation. Hence, RVoG inversion resulted in a low coherence which could not be reliably unwrapped to derive the ground displacement under a canopy. If temporal decorrelation could be mitigated, however, repeat pass polarimetric differential SAR interferometry under a vegetation canopy is feasible.

Coherence optimization in the context of DInSAR in a natural terrain has practical uses in determining hazards from volcanic eruptions and earthquakes. In densely vegetated regions, even though classical DInSAR cannot be applied because of temporal decorrelation, selective processing of coherent pixels with stable scattering mechanism in multi-temporal InSAR context will yield superior results as compared to conventional single polarization channels. In multi-temporal InSAR analysis pixels are selected for parameter estimation based on their quality. Thus coherence optimization increases the number of pixel candidates that are available for processing because the candidate points are denser. Consequently, denser points will give a more robust model fitting because of more individual connections between candidate points making the deformation measurements more reliable.

6. Conclusions

We conclude that ESM provided the highest phase quality improvement, followed by JD and BEST when optimizing quadpol data sets in bare and sparsely vegetated regions. In densely vegetated regions ESM attained the highest signal to noise ratio whereas the phase center of HH-VV polarization channel was closest to the ground surface. In addition, ESM was least affected by phase bias as compared to HH polarization in bare and sparsely vegetated regions. A similar trend was observed when optimizing dual polarized data sets: the TERRASAR-X configuration performed better than the ALOS PALSAR configuration, despite reduced data dimensions. Finally, ESM deformation results showed the highest correlation with the continuous GPS measurements, even though DEM, orbital and atmospheric phase errors were not corrected. Hence, polarimetric optimization coupled with DInSAR analysis yielded more reliable deformation results as compared with HH polarization in a low coherence region.

Acknowledgments

This research work was supported by the Ethiopian government under project number INSA9/JT3/1213/13. The authors wish to thank the European Space Agency (ESA) for providing the ALOS PALSAR data used in this research under the project number 20930. The authors also wish to thank UNAVCO for providing the continuous GPS data and Dr. Robert King of Massachusetts Institute of Technology (MIT) for his help in processing the data. The authors would like to express appreciation to the reviewers for the comments and suggestions, which have improved the quality of the manuscript.

References

Alipour, S., Tiampo, K.F., Samsonov, S.V., González, P.J., 2015. Short-term surface deformation on the Northern Hayward Fault, CA, and nearby landslides using polarimetric SAR interferometry (PolInSAR). Pure Appl. Geophys. 172 (8), 2179–2193.
Altamimi, Z., Collilieux, X., Métivier, L., 2011. ITRF2008: an improved solution of the international terrestrial reference frame. J. Geod. 85 (8), 457–473.
Amelung, F., Jónsson, S., Zebker, H., Segall, P., 2000. Widespread uplift and 'trapdoor' faulting on Galapagos volcanoes observed with RADAR interferometry. Nature 407 (6807), 993–996.
Buckreuss, S., Balzer, W., Mühlbauer, P., Werninghaus, R., Pitz, W.,2003. The TerraSAR-X satellite project. In: IEEE International Geoscience and Remote Sensing Symposium, IGARSS, vol. 5. IEEE, pp. 3096–3098.
Chen, C.W., Zebker, H.A., 2002. Phase unwrapping for large SAR interferograms: statistical segmentation and generalized network models. IEEE Trans. Geosci. Remote Sens. 40 (8), 1709–1719.
Cloude, S.R., Papathanassiou, K.P., 1998. Polarimetric SAR interferometry. IEEE Trans. Geosci. Remote Sens. 36 (5), 1551–1565.
Cloude, S., Papathanassiou, K., 2003. Three-stage inversion process for polarimetric SAR interferometry. IEEE Proc. Radar Sonar Navig. 150 (3), 125–134.
Cloude, S., 2009. Polarisation: Applications in Remote Sensing. Oxford University Press.
Colin, E., Titin-Schnaider, C., Tabbara, W., 2006. An interferometric coherence optimization method in RADAR polarimetry for high-resolution imagery. IEEE Trans. Geosci. Remote Sens. 44 (1), 167–175.
Ferretti, A., Prati, C., Rocca, F., 2001. Permanent scatterers in SAR interferometry. IEEE Trans. Geosci. Remote Sens. 39 (1), 8–20.
Ferro-Famil, L., Neumann, M., Huang, Y., 2009. Multi-baseline POL-InSAR statistical techniques for the characterization of distributed media. In: IEEE International Geoscience and Remote Sensing Symposium, IGARSS, vol. 3, pp. 971–974.
Hammond, J., Kendall, J.-M., Stuart, G., Keir, D., Ebinger, C., Ayele, A., Belachew, M., 2011. The nature of the crust beneath the afar triple junction: evidence from receiver functions. Geochem. Geophys. Geosyst. 12 (12), 1–24.
Hanssen, R.F., 2001. RADAR Interferometry: Data Interpretation and Error Analysis, vol. 2. Springer Science & Business Media.
Iglesias, R., Monells, D., Fabregas, X., Mallorqui, J.J., Aguasca, A., Lopez-Martinez, C., 2014. Phase quality optimization in polarimetric differential SAR interferometry. IEEE Trans. Geosci. Remote Sens. 52 (5), 2875–2888.
Iglesias, R., Monells, D., Lopez-Martinez, C., Mallorqui, J.J., Fabregas, X., Aguasca, A., 2015. Polarimetric optimization of temporal sublook coherence for DInSAR applications. IEEE Geosci. Remote Sens. Lett. 12 (1), 87–91.
Keir, D., Pagli, C., Bastow, I.D., Ayele, A., 2011. The magma-assisted removal of Arabia in Afar: evidence from dike injection in the Ethiopian rift captured using InSAR and seismicity. Tectonics 30 (2), 1–13.
King, R., Bock, Y., 2002. Documentation for the GAMIT GPS Processing Software Release 10.2. Massachusetts Institute of Technology, Cambridge, MA.
Massonnet, D., Rossi, M., Carmona, C., Adragna, F., Peltzer, G., Feigl, K., Rabaute, T., 1993. The displacement field of the landers earthquake mapped by RADAR interferometry. Nature 364 (6433), 138–142.
Mora, O., Mallorqui, J.J., Broquetas, A., 2003. Linear and nonlinear terrain deformation maps from a reduced set of interferometric SAR images. IEEE Trans. Geosci. Remote Sens. 41 (10), 2243–2253.
Morena, L., James, K., Beck, J., 2004. An introduction to the RADARSAT-2 mission. Can. J. Remote Sens. 30 (3), 221–234.
Navarro-Sanchez, V.D., Lopez-Sanchez, J.M., 2012. Improvement of persistent-scatterer interferometry performance by means of a polarimetric optimization. IEEE Geosci. Remote Sens. Lett. 9 (4), 609–613.
Navarro-Sanchez, V.D., Lopez-Sanchez, J.M., Vicente-Guijalba, F., 2010. A contribution of polarimetry to satellite differential SAR interferometry: increasing the number of pixel candidates. IEEE Geosci. Remote Sens. Lett. 7 (2), 276–280.

Navarro-Sanchez, V.D., Lopez-Sanchez, J.M., Ferro-Famil, L., 2014. Polarimetric approaches for persistent scatterers interferometry. IEEE Trans. Geosci. Remote Sens. 52 (3), 1667–1676.

Neumann, M., Ferro-Famil, L., Reigber, A., 2008. Multibaseline polarimetric SAR interferometry coherence optimization. IEEE Geosci. Remote Sens. Lett. 5 (1), 93–97.

Papathanassiou, K.P., Cloude, S.R., 2001. Single-baseline polarimetric SAR interferometry. IEEE Trans. Geosci. Remote Sens. 39 (11), 2352–2363.

Pipia, L., Fabregas, X., Aguasca, A., Lopez-Martinez, C., Duque, S., Mallorqui, J.J., Marturia, J., 2009. Polarimetric differential SAR interferometry: first results with ground-based measurements. IEEE Geosci. Remote Sens. Lett. 6 (1), 167–171.

Rosenqvist, A., Shimada, M., Ito, N., Watanabe, M., 2007. ALO PALSAR: a pathfinder mission for global-scale monitoring of the environment. IEEE Trans. Geosci. Remote Sens. 45 (11), 3307–3316.

Tabb, M., Orrey, J., Flynn, T., Carande, R., 2002. Phase diversity: a decomposition for vegetation parameter estimation using polarimetric SAR interferometry. In: Proceedings of EUSAR 2002, vol. 2, pp. 721–724.

Touzi, R., Lopes, A., Bruniquel, J., Vachon, P.W., 1999. Coherence estimation for SAR imagery. IEEE Trans. Geosci. Remote Sens. 37 (1), 135–149.

UNAVCO, 2016. GNSS Data Archive Interface Version 2 (DAI v2). http://www.unavco.org/data/gps-gnss/data-access-methods/dai2/app/dai2.html (accessed: 07.01.16).

Wu, B., Tong, L., Chen, Y., He, L., 2015. New methods in multibaseline polarimetric SAR interferometry coherence optimization. IEEE Geosci. Remote Sens. Lett. 12 (10), 2016–2020.

Zebker, H., Villasenor, J., et al., 1992. Decorrelation in interferometric RADAR echoes. IEEE Trans. Geosci. Remote Sens. 30 (5), 950–959.